American Journal of Fluid Dynamics 2018, 8(3): 73-83
DOI: 10.5923/j.ajfd.20180803.01

Hydrodynamic Performance of a Novel Ocean Wave Energy Converter

Aliakbar Babajani

Department of Mechanical Engineering, Shahrekord University, Shahrekord, Iran

Abstract Ocean waves are one of the energy resources which have potential to fulfil some parts of the world's energy requirements. Recently, existing OWECs have been evaluated to find the most appropriate systems for the wave energy extraction of the Caspian Sea. Hence, point absorbers are found to be the most appropriate devices for this sea. Generally, the aim of this study is to study a novel ocean wave energy converter named "Searaser" which may be economical and practical for the Caspian Sea. Thus, this study presents a numerical simulation of Searaser inside a wave tank using commercial software (Flow-3D). In order to validate the simulations, the numerical and experimental results were compared with a point absorber and the both were in reasonable agreement. Afterwards, the performance of Searaser was numerically calculated for different heights of ocean waves. Accordingly, the obtained results indicate that the output flow rate and the power generation increase significantly by increment of wave heights, and using this device may have the potential to be practical and profitable for industrial applications by improving its system.

Keywords Searaser, Ocean Wave Energy Converter (OWEC), Computational Fluid Dynamics (CFD), Renewable Energy, Flow-3D

1. Introduction

Fossil fuels as the major source of energy have several disadvantages like environmental hazards, rising prices, climate change. On the other hand, renewable energies such as ocean wave energy, solar energy, and wind energy are sustainable sources which will never run out. Furthermore, these types of energy sources generate electricity without producing any hazardous products such as carbon dioxide (CO_2) or any other chemical pollutants, so they can supply the worldwide demands of electricity. In recent years, the wave energy as a renewable energy has attracted the interest of many researchers and companies due to its incredible advantages. Wave energies have several benefits in comparison with other renewable energies, for instance they are more available, predictable, and higher energy densities, which can produce more power with lower cost. To capture the flow field, some methods are used including computational fluid dynamics [1] for different applications such as heat transfer [2-4] and turbomachinery [5, 6] or other techniques using image processing [7-9] which they have shown a good agreement between numerical and experimental results. The main reason why the numerical approach is used in this research is to evaluate the capability of Flow-3D for energy convertor, since experimental tests are very expensive. Therefore, numerical simulation can be a solution to minimize the costs.

In general, there are diverse types of wave energy converter (WEC) systems. WEC is categorized in four different groups including oscillating water column, overtopping device, attenuator, and point absorber [10]. In the first group, the oscillating water column (OWC) operates on the principle of air compression and decompression. In fact, the air compression and decompression drive the turbine by rising and descending the water in the chamber. For example, spare buoy is a simple form of oscillating water columns [11]. Recently, some theoretical optimization studies have carried out for spare buoys [12, 13]. The best known turbines for OWCs are Wells and Impulse turbines [11]. Falco et al. [14, 15] compared Wells turbine and new biradial Impulse turbine. The result showed that single stage Wells turbines do not have high efficiency for this case and biradial turbines are the best choice in terms of performance.

In the second group, the overtopping devices utilize the wave velocity for filling a reservoir located in the higher level than the ocean surface, and then the water falls in low-head turbines to produce electricity. Some familiar examples of overtopping devices are Wave Dragon [16], SSG [17-19] and WaveCat [20]. Additionally, a new type of overtopping device named overtopping breakwater for

* Corresponding author:
babajani.aliakbar@yahoo.com (Aliakbar Babajani)
Published online at http://journal.sapub.org/ajfd

energy conversional (OBREC) is under development which includes the rubble mound breakwater with frontal reservoir. Diego et al. [21] compared the result of this innovative WEC with traditional rubble mound overtopping device, proposed new formulae for hydraulic performance, and loading on the front reservoir.

In the third group, the attenuators have multiple floating segments connected to each other and these buoys are parallel to the wave direction. In fact, the waves cause the segments to move relative to each other, which this motion concentrated at the joints is used to pump high pressure oil through hydraulic motors and these motors drive electrical generators to produce electricity. Pelamis is a snake-like device that consists of cylindrical bodies connected together [22]. Furthermore, there are other famous attenuators such as Wave Star [23], Salter Duck and Anaconda [24].

In the last group, the point absorbers convert energy by capturing the wave's heaving motion. In fact, the buoys employ the vertical motion of waves to compress gas or liquid; then this fluid drives the power generator and produce electricity. Totally, point absorbers can be divided into single-body or multiple-body devices. Single-body point absorbers move through a fixed seabed case and multiple-body devices generate electricity by motion of two bodies relative to each other [25]. In comparison to other types of WECs, point absorbers are simple and small devices which can be used in different depths of water in offshore areas. In addition, many researchers have focused on modeling the point absorbers to find this system as the most cost-efficient technology of wave energy extraction [26], and It has been proved that the best usable system in the Caspian Sea (specifically in the southern basin) is a point absorber [24]. To produce considerable energy, point absorbers can be attached to each other in parallel or series forms [26, 27]. Over the past decade, many studies have been carried out to investigate the hydrodynamic performances of energy converters; however, recent researches indicate that using numerical is capable of measuring noise generation due to pressure fluctuations [28, 29], and it is necessary to employ these techniques for energy converters in the future.

In 2013, Alivin Smith [30] invented a novel OWEC named "Searaser" based on the registered patent. According to the inventor's patent, this invention has exceptional benefits in compared with other type of OWECs, which will be completely mentioned in section 2 (Description of Searaser). In the current study, the performance of Searaser in a wave tank was studied by solving Navier-Stokes equations. Hence, a commercial CFD code (Flow-3D) which is appropriate for numerical modeling of WEC has been used to solve the governing equations. One can also use other multiphasic software such as Abaqus for this purpose which offers a variety of user friendly subroutines [31, 32]. In order to validate the hydrodynamic results, the hydrodynamic performance of a point absorber was calculated by this software which the difference of numerical and experimental data was acceptable. Afterwards, the performance of Searaser with geometric dimensions based on the extracted data from patent was numerically evaluated for varied wave heights. Eventually, the obtained results demonstrate that the power generation obviously increases by the increment of wave heights.

2. Description of Searaser

This novel technology named "Searaser" which can be used as a water pump to generate electricity was invented by Alvin Smith and registered as a patent [30]. Indeed, Searaser is a new device in order for utilizing hydro-power as a renewable energy source. As shown in Fig.1, Searaser consists of a cylinder attached to a piston. This piston is forced upwards by the buoyancy force since it is floating on the water surface when the ocean waves approach the device. Afterward, the gravity force of body overcomes other forces such as dynamic forces and wall friction after passing waves, and it causes to move buoy downward gradually.

According to the Fig. 2, it employs the periodic motion of waves to pump the ocean water to higher level (on-shore) in order to store it in the large ponds and generate electricity with a turbine and generator on demand. Searaser has many notable advantages which some of them are mentioned here. Firstly, the price of components goes down because the components producing electricity (turbine and generator) are separated from the Searasers while generating electricity on the ocean surface requires the special components due to the corrosion. Secondly, producing electricity by Searaser is obviously considered green energy since there are no climate gas emissions involved (at least not after construction and installation). As another benefit, it has a simpler design and cheaper components than other wave energy converters which make this invention especial. Additionally, the output water from this device can be transferred to the allocated area designated for the off shore wind turbines and it helps to create a more effective area (Figure 3).

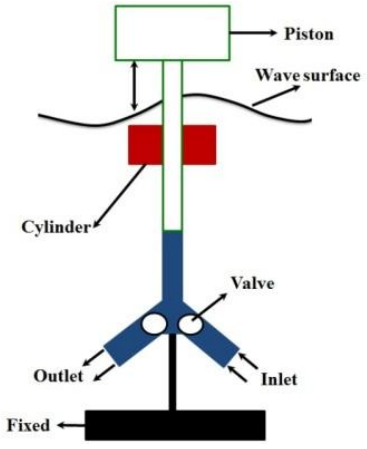

Figure 1. Different components of Searaser

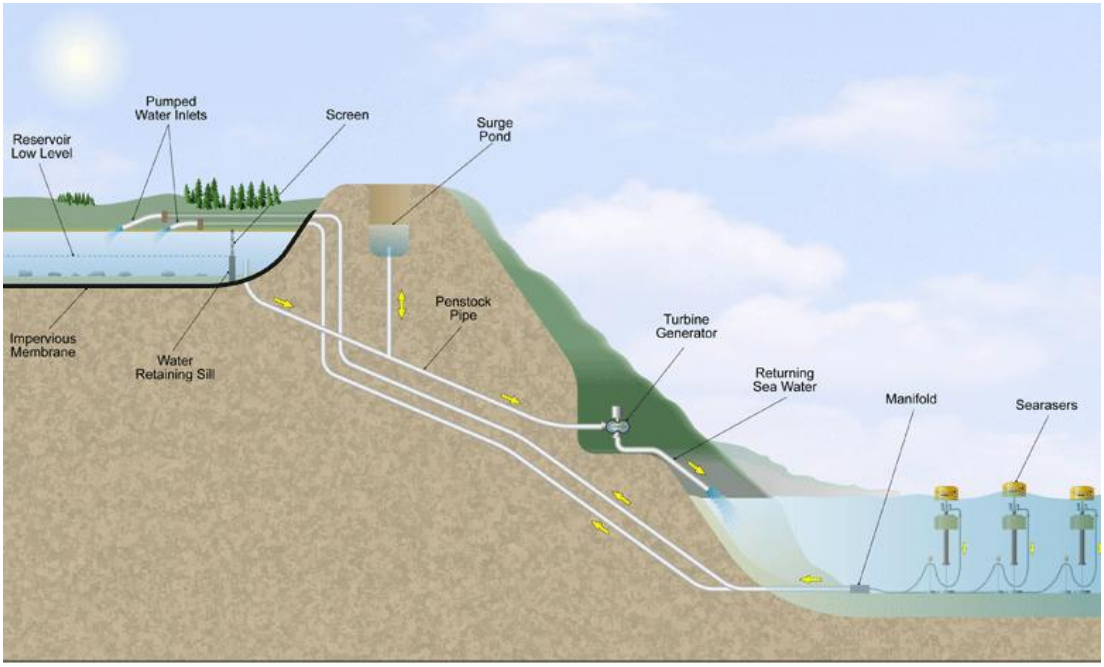

Figure 2. Cycle of electricity generation via Searaser. (www.searaser.net)

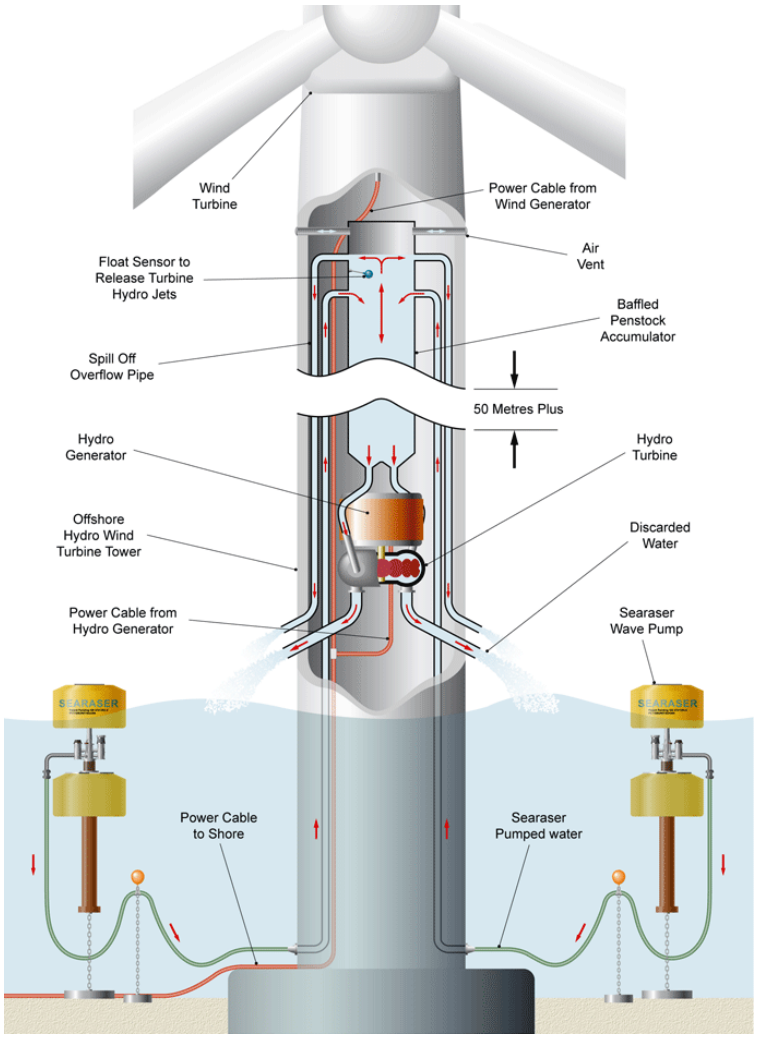

Figure 3. Transferring output water from Searaser inside wind turbine

3. Governing Equations

To perform parametric study and avoid experimental expenses in flow simulation problems [33, 34] numerical approach using Flow-3D was considered. Flow-3D uses a unique technique named FAVOR to describe geometric objects in a computational domain which is based on the concept of area fraction (AF) and volume fraction (VF) in a rectangular structured mesh. The VF is defined as the ratio of open volume to the total volume in a cell whereas three AF's (AFR, AFB, AFT) are defined for three cell faces respectively in the direction of increasing cell-index as the ratio of the open area to the total area. This FAVOR technique works well with complex geometries by introducing the effects of AF and VF into the conservation equations of fluid flow. This technique has led to the successful development of a general moving object (GMO) capability which in principle permits the modelling of any type of rigid body motion (six degree of freedom, fixed axis and fixed point) on a fixed-mesh. This particular simulation is the application of this GMO model to a fixed axis dynamically coupled motion of WRASPA and Searaser. Solver calculates AF and VF at each time step which describes object's motion through a fixed-rectangular mesh. Hydraulic, gravitational, and control forces and torques are calculated and equations of motion for the rigid body are solved explicitly for translational and rotational velocities of moving objects under a coupled motion.

3.1. Equations of Movement (Rigid Body)

In general, each motion of a rigid body can be divided into translational and rotational movements. The velocity of each single moving point is equal to the optional base point velocity plus the velocity that is originated from the rotation of the body around the base point. For movement in 6 degrees of freedom, the general moving object (GMO) model considers the mass center of the body (G) as the base point. The equations for 6 degree of freedom movement are divided into two separate following equations [35]:

$$\vec{F} = \mathrm{m}\frac{d\vec{V}_G}{dt} \tag{1}$$

$$\overrightarrow{T_G} = [\mathrm{J}]\cdot\frac{d\vec{\omega}}{dt} + \vec{\omega}\times([J]\cdot\vec{\omega}) \tag{2}$$

$\vec{\omega}$ is the angular velocity (rad/s), $\overrightarrow{V_G}$ is the velocity of mass center (m/s), $\vec{F}$ is the total force (N), m is the mass of the rigid body(kg), $\overrightarrow{T_G}$ is the total torque (N.m) about G and $[J]$ is the moment of inertia tensor (kg.m^2) about G in a body proportional referenced system. Total force and total torque are calculated as the summation of some different components as follow:

$$\vec{F} = \overrightarrow{F_g} + \overrightarrow{F_h} + \overrightarrow{F_c} + \overrightarrow{F_{nı}} + \vec{F}_i \tag{3}$$

$$\overrightarrow{T_G} = \overrightarrow{T_g} + \overrightarrow{T_h} + \overrightarrow{T_c} + \overrightarrow{T_{nı}} \tag{4}$$

Where $\overrightarrow{F_g}$ is the gravitational force, $\overrightarrow{F_h}$ is the hydraulic force that is due to pressure field and shear forces of the wall on the moving body, $\overrightarrow{F_c}$ is the net control force of the network that can be used for controlling and confining the rigid body motion, $\overrightarrow{F_{nı}}$ is the non-inertial force when the rigid body moves in a non-inertial space system. Therefore, in this case there is no $\overrightarrow{F_{nı}}$, so $\overrightarrow{T_G}$ ،$\overrightarrow{T_g}$ ،$\overrightarrow{T_h}$ ،$\overrightarrow{T_c}$, and $\overrightarrow{T_{nı}}$ are the total torque, gravitational torque, hydraulic torque, control torque and non-inertial torque around the mass center of the rigid body, respectively. The continuity and momentum equations for a moving body and the relative transport equations for the volume of the fluid function (VOF) are as follow:

$$\frac{V_f}{\rho}\frac{\partial\rho}{\partial t} + \frac{1}{\rho}\nabla\cdot(\rho\vec{u}A) = -\frac{\partial V_f}{\partial t} \tag{5}$$

$$\frac{\partial\vec{u}}{\partial t} + \frac{1}{V_f}\left(\vec{u}A_f\cdot\nabla\vec{u}\right) = -\frac{1}{\rho}\left[\nabla \mathrm{p} + \nabla\cdot\left(\tau A_f\right)\right] + \vec{G} \tag{6}$$

$$\frac{\partial F}{\partial t} + \frac{1}{V_f}\nabla\cdot\left(F\vec{u}A_f\right) = -\frac{F}{V_f}\frac{\partial V_f}{\partial t} \tag{7}$$

Where ρ is the fluid density (kg/m^3) (water in this case), $\vec{u}$ is the velocity of fluid (m/s), V_f is the volume fraction, A_f is the area fraction, p pressure (pa), τ the viscous stress tensor (pa), G gravity (m/s^2) and F is the fluid fraction. For coupling of the GMO's motion, equation (1) and (2) should be solved in each time step and the situation of all the objects is recorded and the volume fraction is updated by FAVOR technique. Equation 5 and 6 can be solved by substitution of $(-\partial V_f/\partial \mathrm{t})$ in right- hand side of both equations with the following form:

$$-\frac{\partial V_f}{\partial t} = \overrightarrow{U_{obj}}\cdot\vec{n}S_{obj}/V_{cell} \tag{8}$$

S_{obj}, $\vec{n}$ $\vec{U}_{obj}$ and V_{cell} are the surface area (m^2), surface normal vector, the velocity of moving object (m/s) in a mesh cell and the total cell volume (m^3) respectively. Equation 1 and 2 are solved by the explicit GMO method with the following discretised equations:

$$\vec{F}_h^n + \sum\vec{F}_i = m\left(\frac{\vec{V}_G^{n+1}-\vec{V}_G^n}{\Delta t}\right) \tag{9}$$

$$\vec{T}_h^n + \sum\vec{T}_i = [J]\cdot\left(\frac{\vec{\omega}^{n+1}-\vec{\omega}^n}{\Delta t}\right) + \vec{\omega}^n\times([J]\cdot\vec{\omega}^n) \tag{10}$$

The upper indexes are related to time step, $\sum\vec{F}_i$ and $\sum\vec{T}_i$ are the sum of all force and torque elements except hydraulic parts. In each time step, after calculating $\vec{V}_G^{n+1}$ and $\vec{\omega}^{n+1}$ in the same way, the fluid velocity and pressure field are obtained by duplicately solving the momentum and continuity equations [36].

4. Validation

In order to verify the numerical results in Flow-3D, a point absorber named "WRASPA" was simulated exactly similar to the experimental model in reference [35] to compare the numerical and experimental data. In Fig.4, the geometry and dimensions of simulated WRASPA are shown clearly.

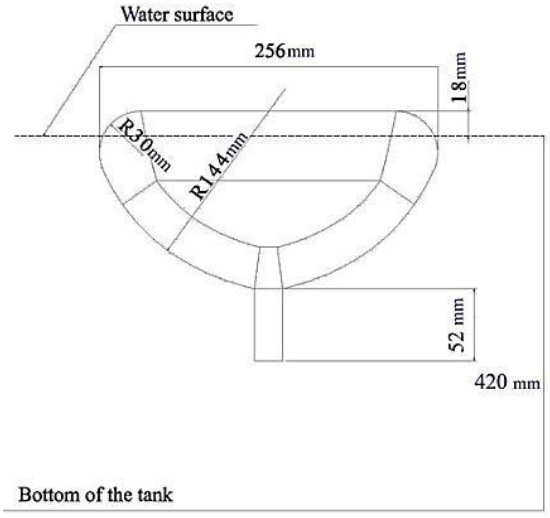

Figure 4. Geometry and dimensions of simulated point absorber (WRASPA)

As it can be seen in Fig.5a, not only were the structured meshes utilized for solution domain, but also two mesh blocks were generated with different sizes to improve the accuracy. In other words, the mesh Block 1 has small grids in which the point absorber was simulated at the middle and the mesh Block 2 has larger grids around the Block 1. In addition, the different boundary conditions considered for this simulation are shown in Fig. 5b completely.

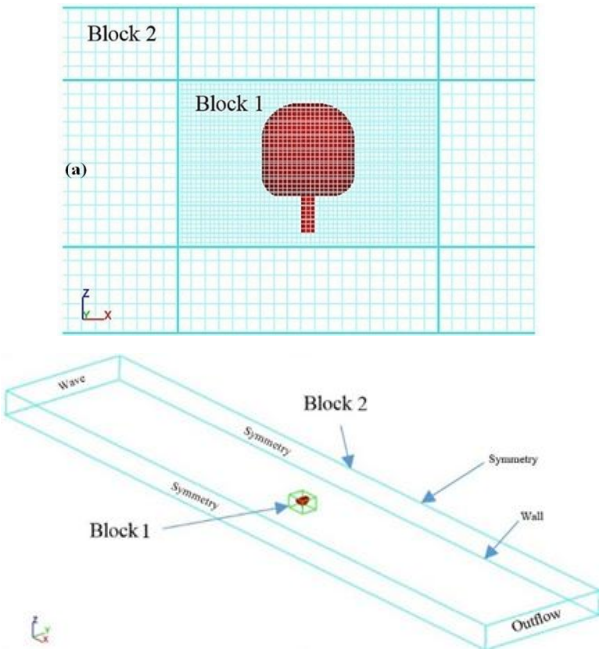

Figure 5. a) Schematic of meshing the wave tank and WRASPA, b) Axis and dimensions including boundary conditions

In this work, the setting parameters include the wave amplitude 0.01m, time period 1s, and water depth 0.42m. The mesh number is 963210 and its smallest grid (0.006m) was generated to model the moving wave inside the tank. As shown in Fig. 6, the wave tank dimensions are 12.5m long, 1.5m wide and 0.45m high. Besides, the RNG (k-ε) turbulence model was employed to solve the turbulent flow because it has acceptable accuracy for this case [37]. The position of buoy (based on the angular movement in radian) for WRASPA is displayed in Fig. 6 which they are in reasonable agreement with each other and their differences can be almost acceptable except for the vicinity of the peaks.

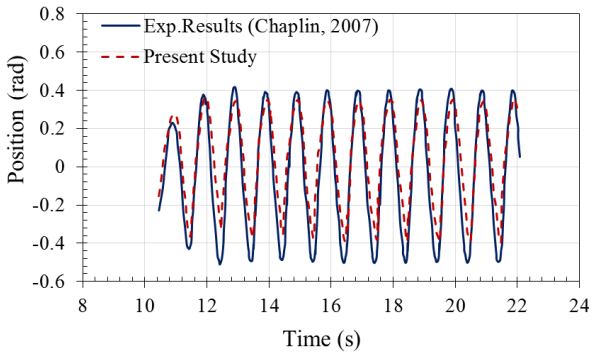

Figure 6. Comparison of numerical and experimental results for angular rotation

As indicated in Fig.7, the velocity contours are different in 1.09s and 15.75s because the velocity is increased when the wave reaches near the buoy and the angular position is changed while wave is passing the point absorber. In Fig.8, the free surface elevation was separately calculated in 1.09s and 6.75s. This plot indicates that the wave shape changes by passing time.

a) t=1.09s

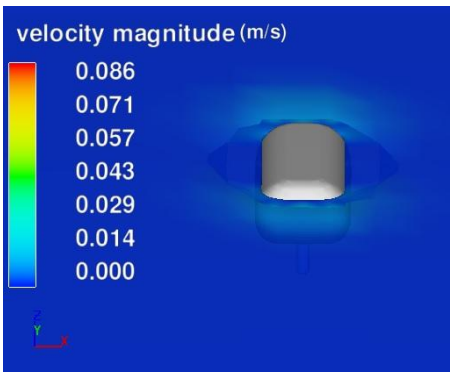

b) t=15.75s

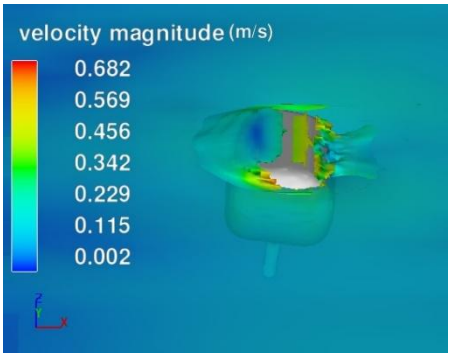

Figure 7. Velocity contour of simulated WRASPA, a) t=1.09s, b) t=15.75s

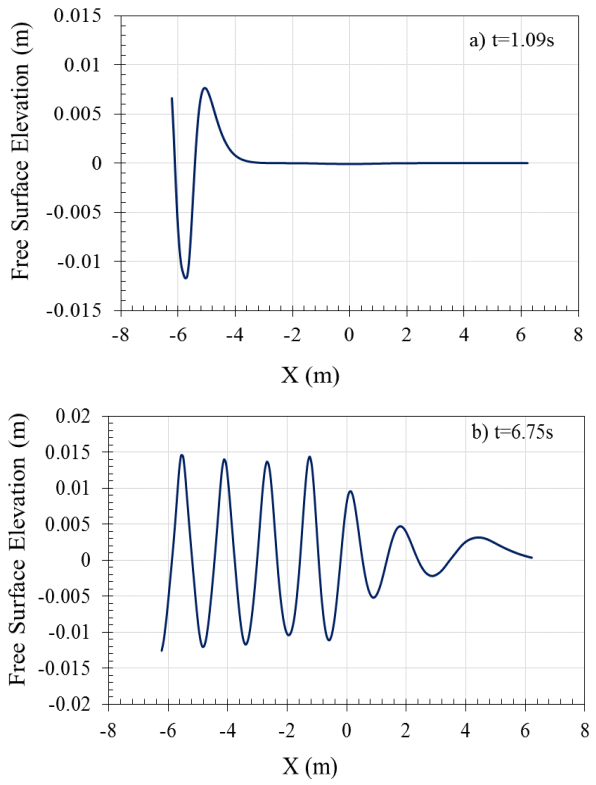

Figure 8. Free surface elevation of wave for different times; a) t=6.75s, b) t=1s

5. Searaser Modeling

5.1. Geometrical Dimensions and Components

In this study, Alvin Smith's second scheme (modified model) was chosen for simulation including 4 main bodies as follow:

a) Buoy

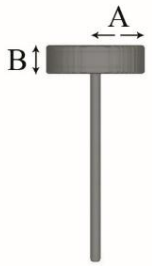

Figure 9. Schematic of first component-buoy

The buoy radius and height are A=2.6m and B=1.5m, respectively. This buoy is inserted 10.1m deep in the pumping duct. The radius of this part is considered equal to radius of the pumping case to prevent leakage from the edges. As shown in Fig.9, the buoy is not completely filled and a cylindrical space with the radius of 2.3m and height of 0.5m is extracted from the buoy. As the buoy should overcome the water column and also push the accumulated water, the net weight of this buoy is 9000kg. In order to construct this device, specific composite material is usually utilized to prevent the corrosion caused by water; also the buoy should be filled with sand, water to have the reasonable weight since the composites are lightweight. Furthermore, the buoy was designed to be capable of moving only in vertical direction (the gravity direction) because the vertical duct does not allow it to move toward other directions.

b) Chamber

According to the Fig.10, the second part is a chamber including inlet and outlet valves with diameter of C=0.536m. The radius and height of the upper cylindrical section are D= 2.1m and E=2m, respectively. In this simulation, the bottom of chamber was fixed because it helps the converter to reach the maximum efficiency. In addition, the assumption of fixed bottom chamber was applied to have a better convergence in the solution process.

Figure 10. Schematic of second component-chamber

c, d) Inlet & outlet valves

In order to select the valve type, three factors should be considered including software limitation for simulation, large diameter of outlet pipe, and valve compatibility to the seawater. According to the research, Wafer Swing Check Valve could be a suitable choice for this valve, which this kind of valve is indicated in Fig.11 schematically. According to the valve catalog of the CLA-VAL company [38], this valve was made of Aluminum Bronze ASTM B148, Alloy 95200, so the density was assigned 7.64 gr⁄cm^3, and the size F and G sections were 0.8m and 0.536m, respectively. The properties of outlet valve were set the same as inlet valve in modeling. As shown in Fig. 11, a circle disk was designed as inlet and outlet valve, and this disk rotates in Y direction (pin) freely similar to figure 11. Therefore, it rotates around Y axis by entering and exiting the water flow.

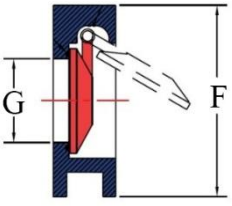

Figure 11. Schematic of outlet and inlet valve- Wafer Swing Check Valve

5.2. Boundary Conditions and Mesh Blocks

In the present work, meshing the solution domain was extremely important because the fluid and solid were moving simultaneously. According to the ability of meshing in this software, three mesh blocks were generated with structure type to improve the accuracy of calculations. As indicated in Fig. 12, X and Y coordinate axes were on the center of upper buoy and Z axis was in direction of ground gravity. In Fig. 12, the abbreviation of WV, S, O, and W stand for wave, symmetry, outflow and wall conditions. In addition, the RNG (k-ε) turbulence model was utilized to model the turbulent flow while the wave was sinusoidal.

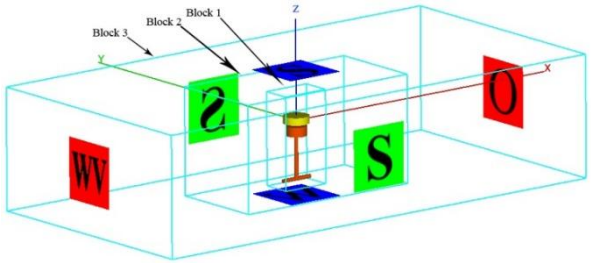

Figure 12. Boundary conditions and mesh blocks

6. Grid Independency

Table 1. Different mesh generation

	Cell number (Block 1)	Mesh block
1	298320	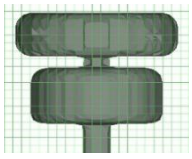
2	504186	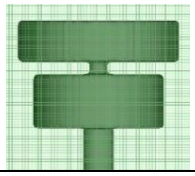
3	723451	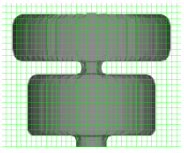
4	904450	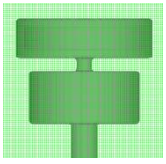

Grid study is usually essential to acquire the number of a sufficient grid. Therefore, four grids were generated with 298320, 504186, 723451, and 904450 cell numbers (Block 1) in order to simulate a 3D Searaser for a moving wave with the height of 1.25m. As shown in Table 1, the numbers of grids were increased in mesh blocks to enhance the accuracy of the solution. In Fig.13, the volume flow rate was measured for various times in the outlet valve. By comparing the curves, it was quite obvious that the grid with 504186 cells was suitable for the present study. Thus, this grid was chosen for all simulations of this research.

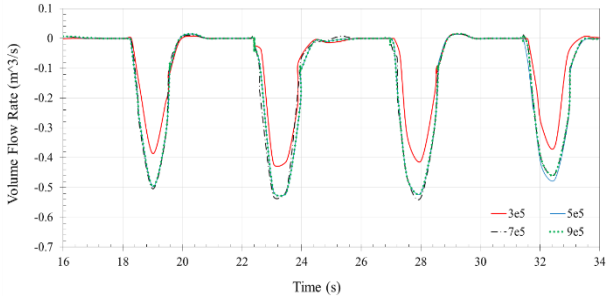

Figure 13. Comparison of outlet volume flow rate for a wave amplitude 1.25m

In Table 2, run time is shown for different cell sizes for time average 17.5s.

Table 2. Run time for different mesh size

Mesh	Total cells	Smallest cell size (m) (Block 1)	Run time for t_{avg} =17.5 sec.
1	963210	0.006	1 day 7hr
2	1516695	0.004	2 days 8hr
3	1952904	0.002	3 days

7. Results and Discussion

In Fig.14, hydrostatic pressure contour was depictured in three dimensions for wave tank. As it can be seen in this figure, the wave generation starts from X_{min} moving toward the X_{max} after passing the Searaser. As shown, hydrostatic pressure increases linearly in the wave tank because the water depth linearly grows up.

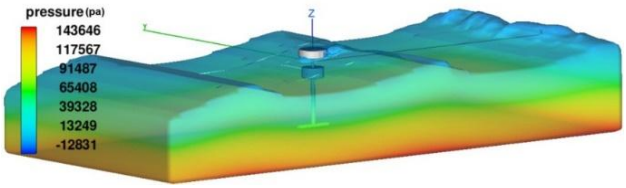

Figure 14. Hydrostatic pressure contour in the wave tank

In Fig. 15, velocity contour is indicated when the water is drawn by inlet valve. By reaching the wave near the upper buoy, the buoy moves upward and causes the water to be drawn into the inlet valve. Afterwards, the buoy goes down when the wave passes the Searaser and the buoy weight causes the water inside the duct to be extracted from outlet valve.

In this section, the performance of Searaser was evaluated for four wave heights including 0.5m, 0.94m, 1.25m and 2.34m, because the wave height for Caspian Sea changes based on the Table 3. The 95th percentile indicated the maximum Hs (wave height) conditions based on the fact

that this is not affected by the extreme outliers that could exist in a dataset. The Mean percentile was also evaluated to indicate the average Hs which happened at southern basin of the Caspian Sea. In this article, the concentration is to examine the influence of wave height on the device operation; therefore, it is necessary to consider one wave period for various wave heights which has the most potential to occur. The wave period varies between 2s and 8s in the southern basin of the Caspian Sea which is equal to 4.5s in average [24]. The displacement of mass center for buoy in Z direction was plotted versus time for each wave height in Fig.16. To check steady state condition, the time domain is chosen 51 seconds. Since the Searaser should be studied at steady state condition and as it is clear in the picture for the first cycles, the waves have not reached the end of the wave tank, so the 3rd cycle is chosen as the base for each wave height.

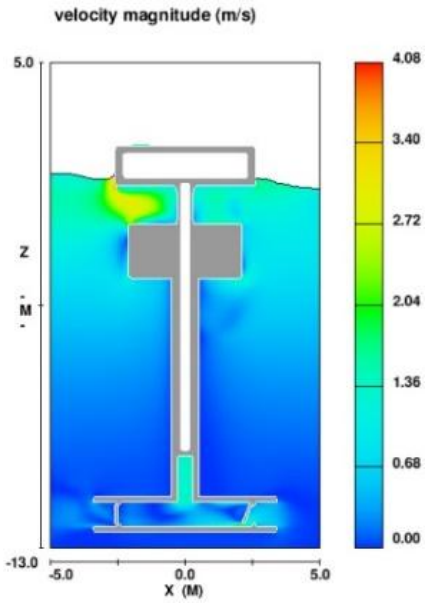

Figure 14. Velocity contour in the suction occasion time 21s

Table 3. Different wave heights for the south of Caspian Sea [39]

Season	Mean (m)	95th (m)
Summer	0.5	1.25
Winter	0.94	2.34

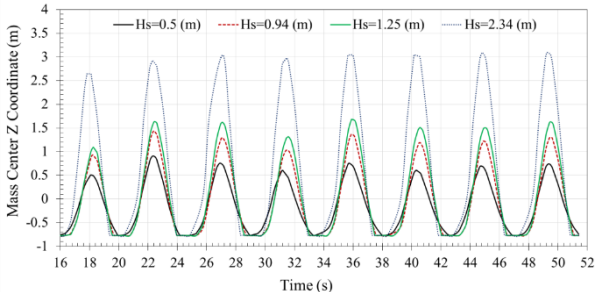

Figure 15. Displacement of mass center for buoy in wave heights 0.5m, 0.94m, 1.25m, and 2.34m

In Fig. 17, the water flow rate exiting from the outlet valve was plotted for four different wave heights in 51s. In this figure, the numbers for the volume flow rate are negative because the direction of outlet flow is the opposite of X axis. By increasing the wave height from 0.5m to 2.34m, the buoy can reach the higher level; hence, the outlet flow rate and the Searaser's efficiency will increase significantly. According to the Fig.17, the curve of volume flow rate is reported after passing the time about 16s, because the moving cycle of buoy will be steady after this time. As it can be seen in the figure, the cycles are repeated each 4.5s which is the same as the time period of wave.

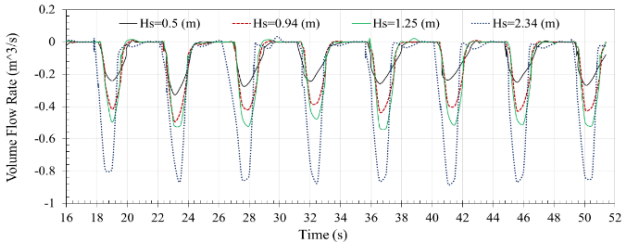

Figure 16. Output volume flow rate from the outlet valve for various times in wave heights 0.5m, 0.94m, 1.25m, and 2.34m

In order for better understanding, pressure contour of Searaser in the wave tank was plotted in figure 18 for different times including 0s, 42.5s, 44s and 45s. Additionally, this figure indicates the movement of ocean wave, outlet and inlet valve at different times.

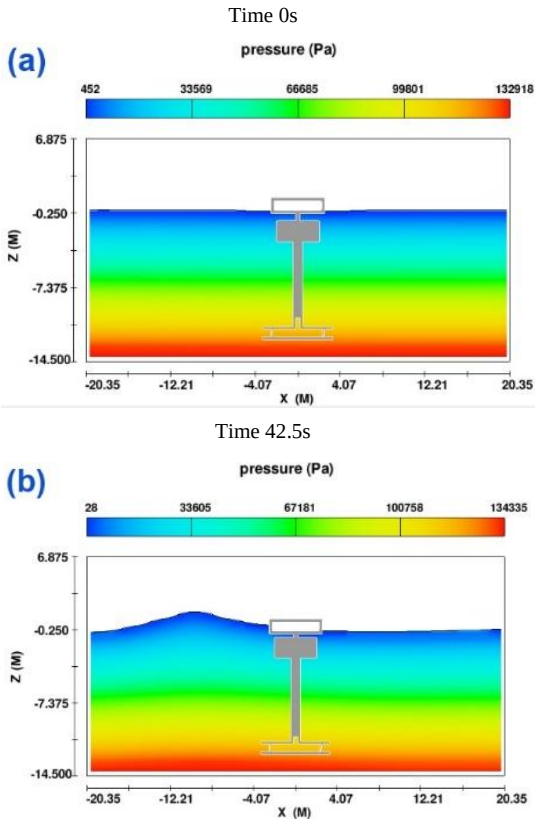

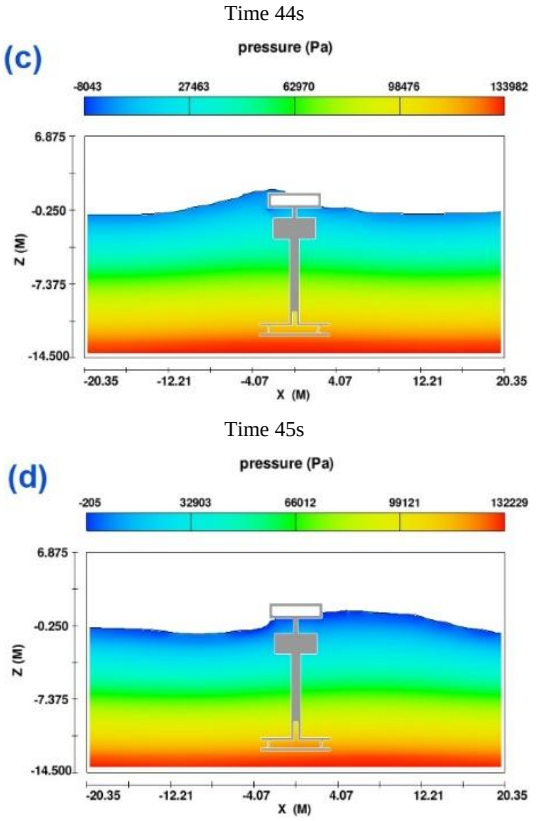

Figure 17. Pressure contour of wave motion at different times 0s, 42.5s, 44s, and 45s

In Fig.19, the output power of Searaser for four wave heights was calculated in different times based on Eq.11. In this equation, A is the outlet area of outflow from the Searaser (m^2), Q is the outlet volume flow rate (m^3/s), and $\dot{P}$ is the output power (w) [40].

$$\dot{P} = \frac{1}{2A^2}\rho Q^3 \quad (11)$$

As it can be seen clearly in this figure, the output power is extremely dependent on the wave height. This plot shows that the device does not have any output power in 4.5s (wave period) because the upper buoy does not have any movement when there is no ocean wave. Therefore, this cycle is repeated periodically for each wave height which is not desirable when the purpose is to produce electricity continuously.

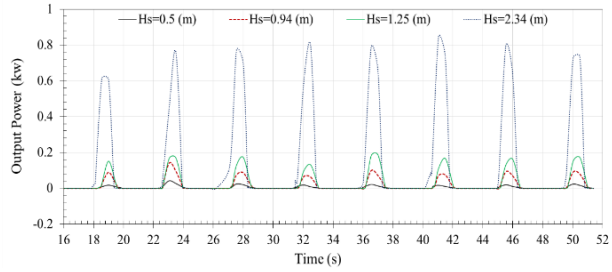

Figure 18. Output power of Searaser for four wave heights

The maximum output power of this device for different wave heights were listed in Table 4. According to this list, the maximum output power in winter and the minimum output power in summer are 0.8kw and 0.02kw, respectively. In comparison with the other wave energy converter similar to this type such as L10 and Upsala, the output power of Searaser is lower [24]. However, this device has less manufacturing costs but it can be placed in large numbers for increasing the output power in an especial area. In Fig. 20, the output power was depicted versus Hs, and its equation is similar the extractable power (Eq. 12), since the power changes with a quadratic equation in both. In order to calculate the extractable power from ocean wave in the Caspian Sea, Eq.12 can be used [24]. In this equation, Hs is wave height (m), T is wave period (s), ρ is water density (kg/m^3), g is gravity (m/s^2), and P is extractable power (w/m).

$$P = \frac{1}{64\pi}\rho g^2 H_s^2 T \quad (12)$$

Table 4. Extractable and output power for Searaser

Wave height (m)	Maximum extractable power (kw/m)	Maximum output power (kw)
0.5	0.54	0.02
0.94	1.9	0.1
1.25	3.37	0.17
2.34	11.79	0.8

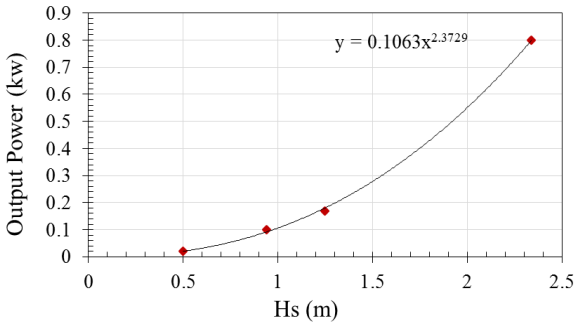

Figure 19. Curve of output power versus Hs

8. Conclusions

In recent years, ocean wave energy converters have been investigated to find the most appropriate system to harvest the wave energy in Caspian Sea. Hence, the commercial software (Flow-3D) was employed to simulate a novel wave energy converter Searaser invented by Alvin Smith. In this simulation, the upper buoy of the converter was designed to move up by the ocean waves generated in a 3D numerical wave tank. Afterwards, some significant parameters of Searaser were computed to capture some parameters such as output fluid flow, extractable wave power, and output power. In fact, these parameters were calculated based on the summer and winter data when the wave heights are variable in Caspian Sea. Consequently, the extractable power and the output power values increase during the winter in comparison with the summer at the same conditions in the Caspian Sea. According to the obtained

results, output power has a non-linear dependency on the wave height. Additionally, the numerical results indicate that each Searaser has excellent potential to pump the ocean water in an upper pool; therefore, this water can be utilized with a Francis turbine to produce electricity on demand.

REFERENCES

[1] Wu X, Sharma A, Jafari M, Sarkar P. Towards Predicting Dry Cable Galloping using Detached Eddy Simulations. In55th AIAA Aerospace Sciences Meeting 2017 (p. 1483).

[2] Hafezisefat P, Esfahany MN, Jafari M. An experimental and numerical study of heat transfer in jacketed vessels by SiO_2 nanofluid. Heat and Mass Transfer. 2017 Jul 1; 53(7): 2395-405.

[3] Ramezani M, Legg MJ, Haghighat A, Li Z, Vigil RD, Olsen MG. Experimental investigation of the effect of ethyl alcohol surfactant on oxygen mass transfer and bubble size distribution in an air-water multiphase Taylor-Couette vortex bioreactor. Chemical Engineering Journal. 2017 Jul 1; 319: 288-96.

[4] Haghighat AK, Roumi S, Madani N, Bahmanpour D, Olsen MG. An intelligent cooling system and control model for improved engine thermal management. Applied Thermal Engineering. 2018 Jan 5; 128: 253-63.

[5] Jafari M, Sojoudi A, Hafezisefat P. Numerical Study of Aeroacoustic Sound on Performance of Bladeless Fan. Chinese Journal of Mechanical Engineering. 2017 Mar 1; 30(2): 483-94.

[6] Jafari M, Afshin H, Farhanieh B, Bozorgasareh H. Numerical aerodynamic evaluation and noise investigation of a bladeless fan. Journal of Applied Fluid Mechanics. 2015 Jan 1; 8(1): 133-42.

[7] Poddar S, Ozcan K, Chakraborty P, Ahsani V, Sharma A, Sarkar S. Comparison of Machine Learning Algorithms to Determine Traffic Congestion from Camera Images. 2018.

[8] Sharma A, Ahsani V, Rawat S. Evaluation of Opportunities and Challenges of Using INRIX Data for Real-Time Performance Monitoring and Historical Trend Assessment.

[9] Chakraborty P, Adu-Gyamfi YO, Poddar S, Ahsani V, Sharma A, Sarkar S. Traffic Congestion Detection from Camera Images Using Deep Convolution Neural Networks. 2018.

[10] Brekken TK, Von Jouanne A, Han HY. Ocean wave energy overview and research at Oregon State University. In Power Electronics and Machines in Wind Applications, 2009. PEMWA 2009. IEEE 2009 Jun 24 (pp. 1-7). IEEE.

[11] Falcão AF, Henriques JC, Gato LM, Gomes RP. Air turbine choice and optimization for floating oscillating-water-column wave energy converter. Ocean engineering. 2014 Jan 1; 75: 148-56.

[12] Gomes RP, Henriques JC, Gato LM, Falcão AD. Hydrodynamic optimization of an axisymmetric floating oscillating water column for wave energy conversion. Renewable Energy. 2012 Aug 1; 44: 328-39.

[13] Falcão AF, Henriques JC, Cândido JJ. Dynamics and optimization of the OWC spar buoy wave energy converter. Renewable energy. 2012 Dec 1; 48: 369-81.

[14] Falcão AF, Gato LM, Nunes EP. A novel radial self-rectifying air turbine for use in wave energy converters. Renewable Energy. 2013 Feb 1; 50: 289-98.

[15] Falcão AD, Gato LM, Nunes EP. A novel radial self-rectifying air turbine for use in wave energy converters. Part 2. Results from model testing. Renewable energy. 2013 May 1; 53: 159-64.

[16] Kofoed JP, Frigaard P, Friis-Madsen E, Sørensen HC. Prototype testing of the wave energy converter wave dragon. Renewable energy. 2006 Feb 1; 31(2): 181-9.

[17] Vicinanza D, Frigaard P. Wave pressure acting on a seawave slot-cone generator. Coastal Engineering. 2008 Jun 1; 55(6): 553-68.

[18] Vicinanza D, Ciardulli F, Buccino M, Calabrese M, Koefed JP. Wave loadings acting on an innovative breakwater for energy production. Journal of Coastal Research. 2011(64): 608.

[19] Vicinanza D, Margheritini L, Kofoed JP, Buccino M. The SSG wave energy converter: Performance, status and recent developments. Energies. 2012 Jan 31; 5(2): 193-226.

[20] Fernandez H, Iglesias G, Carballo R, Castro A, Fraguela JA, Taveira-Pinto F, Sanchez M. The new wave energy converter WaveCat: Concept and laboratory tests. Marine structures. 2012 Dec 1; 29(1): 58-70.

[21] Vicinanza D, Contestabile P, Nørgaard JQ, Andersen TL. Innovative rubble mound breakwaters for overtopping wave energy conversion. Coastal Engineering. 2014 Jun 1; 88: 154-70.

[22] Dalton GJ, Alcorn R, Lewis T. Case study feasibility analysis of the Pelamis wave energy convertor in Ireland, Portugal and North America. Renewable Energy. 2010 Feb 1; 35(2): 443-55.

[23] Antonio FD. Wave energy utilization: A review of the technologies. Renewable and sustainable energy reviews. 2010 Apr 1; 14(3): 899-918.

[24] Alamian, R., Shafaghat, R., Miri, S. J., Yazdanshenas, N., Shakeri, M. (2014). Evaluation of Technologies for Harvesting Wave Energy in Caspian Sea. Renewable and Sustainable Energy Reviews, 32, 468-476.

[25] Pastor J, Liu Y. Frequency and time domain modeling and power output for a heaving point absorber wave energy converter. International Journal of Energy and Environmental Engineering. 2014 Jul 1; 5(2-3): 101.

[26] Li Y, Yu YH. A synthesis of numerical methods for modeling wave energy converter-point absorbers. Renewable and Sustainable Energy Reviews. 2012 Aug 1; 16(6): 4352-64.

[27] Babajani AA, Jafari M, Sefat PH. Numerical investigation of distance effect between two Searasers for hydrodynamic performance. Alexandria Engineering Journal. 2016 Sep 1; 55(3): 2257-68.

[28] Jafari M, Afshin H, Farhanieh B, Bozorgasareh H. Experimental and Numerical Investigation of a 60cm

Diameter Bladeless Fan. Journal of Applied Fluid Mechanics. 2016 Apr 1; 9(2).

[29] Jafari M, Afshin H, Farhanieh B, Sojoudi A. Numerical investigation of geometric parameter effects on the aerodynamic performance of a Bladeless fan. Alexandria Engineering Journal. 2016 Mar 1; 55(1): 223-33.

[30] Smith, A., "PUMPING DEVICE", Patent Application Publication, US 2013/0052042 A1, 2013.

[31] Kamrani M, Levitas VI, Feng B. FEM simulation of large deformation of copper in the quasi-constrain high-pressure-torsion setup. Materials Science and Engineering: A. 2017 Sep 29; 705: 219-30.

[32] Kamrani M, Feng B, Levitas VI. Modeling of Strain-Induced Phase Transformations Under High Pressure and Shear. In Proceedings of the International Conference on Martensitic Transformations: Chicago 2018 (pp. 47-51). Springer, Cham.

[33] Razavi A, Sarkar PP. Tornado-induced wind loads on a low-rise building: Influence of swirl ratio, translation speed and building parameters. Engineering Structures. 2018 Jul 15; 167: 1-2.

[34] Razavi A, Sarkar PP. Laboratory Study of Topographic Effects on the Near-surface Tornado Flow Field. Boundary-Layer Meteorology. 2018 Mar: 1-24.

[35] Bhinder M, Mingham C, Causon D, Rahmati M, Aggidis G, Chaplin R. Numerical and experimental study of a surging point absorber wave energy converter. In Proceedings of the 8th European wave and tidal energy conference 2009.

[36] Hirt, C. W., Nichols, B. Flow-3D User's Manual. Flow Science Inc. (1988).

[37] Choi BH, Kim DC, Pelinovsky E, Woo SB. Three-dimensional simulation of tsunami run-up around conical island. Coastal Engineering. 2007 Aug 1; 54(8): 618-29.

[38] Cla-Val company; Wafer Swing Check Valve; www.cla-val.com.

[39] Rusu E, Onea F. Evaluation of the wind and wave energy along the Caspian Sea. Energy. 2013 Feb 1; 50: 1-4.

[40] Fox, R. W., McDonald, A. T., Pritchard, P. J.. Introduction to Fluid Mechanics (Vol. 7), New York: John Wiley & Sons. 1985.